Phase-Field Simulation of Hydraulic Fracturing by CO_2, Water and Nitrogen in 2D and Comparison With Laboratory Data

Yixuan Feng[1] [ID], **Kjetil Haugen[1], and Abbas Firoozabadi[1]** [ID]

[1]Department of Chemical and Biomolecular Engineering, Rice University, Houston, TX, USA

Abstract Hydraulic fracturing of tight subsurface formations has mainly been conducted using water. Waterless hydraulic fracturing by CO_2 may have advantages over fracturing by water. The challenge has been numerical simulation of the process. In this work, we conduct a comprehensive study on 2D hydraulic fracturing simulation by water, CO_2, and nitrogen. The simulations are based on the phase-field; the results are compared with the lab data. We first present advances in simulation of fluid exchange between the fractures and the rock matrix. The conventional nodal-based finite element method may give rise to unphysical negative pressure around the tip and fracture notch. We demonstrate that the mixed hybrid finite element method gives non-negative pressure distribution. Next, we examine the effect of inertial term on fracture configuration and observe branching by CO_2 under dynamic formulation with a low critical energy release rate. Lastly, we find from our simulations that in shale rocks, the critical energy release rate is the lowest for CO_2, followed by nitrogen, and then water. Consequently, CO_2 provides the highest fracture surface area and fracture intensity. In a sandstone sample we find nitrogen has a lower energy release rate than water. As a result, the fracture surface area is higher for nitrogen than water. Our simulation results confirm that the phase-field method may incorporate fluid-rock surface free energy without the need for various parameter adjustments.

Plain Language Summary To increase oil and gas production rate, water is injected in wells to fracture the rocks to create the new paths for flow. Water is selected due to availability and despite the fact that it has many environmental issues. It has been known for some years that water may damage some reservoir rocks and fracturing may not be extensive. Most models for numerical simulation of fracturing are based on simple knowledge of solid mechanics which only relates to effective stress. These models may not describe the effect of type of fluids. In this study, we investigate the use of CO_2 as the fracturing fluid through simulations and compare the results with laboratory experiments. We use the phase-field which allows approximation of discrete fractures by a continuous variable. We examine the breakdown pressure and the fracture pattern induced by different fluids. For water, the breakdown pressure is the highest compared to CO_2 and nitrogen. CO_2 has the lowest breakdown pressure. The fracture intensity and fracture surface are the highest for CO_2 compared to water and nitrogen. In this work, we include rock acceleration in numerical solution of rock momentum balance with flow and improve the accuracy of pressure prediction through mixed hybrid finite element.

1. Introduction

Hydraulic fracturing by pressurized water is widely used in stimulation of wells in bedrock formations. The method requires an enormous amount of water and introduces many potential environmental issues in relation to fresh water consumption and potential contamination of drinking water supplies (Thomas et al., 2019). CO_2 is considered a more environmentally friendly alternative because it adsorbs to the rock surface, has no flowback, and does not block pores (Middleton et al., 2015). Moreover, water-based fluids tend to be trapped in formations, inhibiting oil- and gas-phase flow due to clay-mineral swelling which reduces permeability. CO_2 fracturing is a promising alternative as it results in a lower breakdown pressure and creates more extensive fractures, which increases gas and oil production rate. In recent years, hydraulic fracturing by water and by CO_2 has been extensively studied in the laboratory. In the field scale, one comprehensive trial by CO_2 for fracturing and viscosified CO_2 for proppant placement has been conducted in an

oil field in which water fracturing has not been effective. The production data demonstrate effectiveness of CO_2 fracturing compared to water fracturing (Song et al., 2019).

Both discrete and continuous approaches have been used in numerical modeling of hydraulic fracturing. The discrete approach introduces discontinuities by explicit representation of the geometry (Li et al., 2020; Li & Zhang, 2018; Urban-Rascon & Aguilera, 2020). In the discrete approach some authors have used the cohesive zone model to examine the separation of the fracture surfaces at the tip (Carrier & Granet, 2012; Chen et al., 2009). There are two continuous approaches in numerical simulation of fracturing. One is based on the damage evolution law that examines the stress condition of rock using failure criteria in relation to fracture creation and propagation. The other approach is the phase-field, which is based on the idea of surface energy density related to the critical energy release rate and the minimization of the Lagrange energy functional. Both methods approximate the discontinuities in a transition region, allowing efficient numerical modeling of complex crack topologies. There have been several comprehensive studies presenting both approaches. Liu, Zhu, et al. (2018) apply the damage evolution law to simulate water, liquid CO_2, and supercritical CO_2 fracturing of shale formations. The fracture patterns induced by supercritical CO_2 are more complex and more widely distributed than those induced by liquid CO_2 and water. The authors suggest that a lower dynamic viscosity results in extensive fracturing. The effect of dynamic viscosity on fracturing and the effect of initial pressure on breakdown pressure are also studied through sensitivity analysis. Wang and Zhang (2018) also apply the damage evolution law to simulate water, nitrogen, and supercritical CO_2 fracturing in shale. The damage by tensile stress is suggested to be the major mode of rock failure. The authors examine the effect of boundary stress and report that more fractures are induced when the boundary stresses in two perpendicular directions are the same; the main fracture propagates along the maximal principal stress direction and the fracture pattern is the most complex in the isotropic stress state. Zhou et al. (2019) simulate water fracturing in 2D and 3D using the phase-field. They investigate the effect of injection rate on breakdown pressure and fracture pattern. The breakdown pressure is slightly higher and branching occurs closer to the notch at a higher injection rate. The interaction between induced fractures and natural fractures is also simulated. Wheeler et al. (2020) have developed the IPACS (Integrated Phase-field Advanced Crack Propagation Simulator) to model heterogeneous media, multiple initial fractures, multiple injection points, natural fractures, and proppant transport in 3D. The Galerkin finite element is employed for the spatial discretization of all variables. The numerical robustness is shown through qualitative computational analysis.

In the cohesive zone model, fracture initiates when the cohesive stress attains a critical value, and fracture opening is resisted by cohesive stress until a critical fracture width is reached (Hillerborg et al., 1976; Ortiz & Pandolfi, 1999). Cohesive stress and fracture width are assumed to have a linear relationship (Alpak, 2021; Dean & Schmidt, 2009; van Dam et al., 2002), and the critical fracture width is determined by the critical cohesive stress and energy release rate G_c, which is the integration of cohesive stress over fracture width. G_c is calculated by stress intensity factor according to linear elastic fracture mechanics (Alpak, 2021). In theory, the cohesive zone model is superior to phase-field and damage evolution law because it considers fracture tip geometry, but it is more difficult to implement in practice, which potentially leads to oversimplification. The critical cohesive stress is obtained from uniaxial tensile test and considered to be the same as tensile strength (van Dam et al., 2002), ignoring the fluid effect. There are three stress intensity factors: Mode-I for normal stress, Mode-II for in-plane shear stress and Mode-III for anti-plane shear stress, but only Mode-I stress intensity factor is considered in the cohesive zone model (Alpak, 2021; Dean & Schmidt, 2009) which neglects fracturing due to shear. The shear failure may not be directly related to fracture width. The cohesive zone model requires fine meshing near fracture tip (Dean & Schmidt, 2009). Alternatively, 2D fracture element is used in 3D simulation where the fracture width is not represented in a mesh (Alpak, 2021).

In the damage evolution law, fractures are initiated when the stress condition reaches the maximum tensile or the shear failure criterion. The damage variable is determined by comparing principal strain to maximum tensile or compressive strain based on failure criteria. The Young's modulus and permeability in the transition zone from rock to fracture is described as a function of the damage variable (Liu, Zhu, et al., 2018; J. Wang et al., 2017; J. G. Wang & Zhang, 2018; Q. Zhang et al., 2019). However, the failure criteria are based on the stress response. The damage variable is calculated based on local strains, which may lead to numerical instability and mesh dependency (Steinke et al., 2016). Some authors combine the concepts of invasion

pressure and fluid-fluid interfacial tension with the damage evolution law (J. Wang et al., 2017). Invasion pressure is defined as the minimum pressure that exceeds capillary exclusion to control fluid flow into the pore space. It is assumed to be proportional to the interfacial tension and the square root of the ratio of porosity to permeability. Fluid flow from the fracture to the rock matrix is assumed to be zero until the fluid injection pressure is higher than the invasion pressure. The use of the concept of invasion pressure allows adjustment in modeling to control the breakdown pressure. However, the use of the concept may not be valid in a single-phase state. There is no meaning to interfacial tension of single-phase fluid, and it has no relation to the solid-fluid interfacial energy. Consequently, there is no justification for using invasion pressure of single phase fluid-rock systems in computing breakdown pressure.

We have selected the phase-field method due to incorporation of Griffith's theory (1921). Griffith proposed that in brittle fracture creation and propagation, the potential energy from tension is converted to surface energy of the created fractures. A phase-field variable has been subsequently introduced to describe fracture energy and the tensile part of the elastic strain energy. The material's resistance to fracture propagation is characterized by the critical energy release rate G_c. In a solid in contact with a fluid, G_c is related to solid-fluid interfacial energy density (Wu & Firoozabadi, 2021). The adsorption of a fluid to rock surface affects the interfacial energy density.

Minimizing the Lagrange energy functional during crack propagation leads to the momentum balance and governing equation in the phase-field. The fluid flow is described based on mass balance. Miehe et al. (2010) present fracture modeling based on brittle state and quasi-static formulation (that is, without consideration of the inertial term in momentum balance) of the phase-field. More recently, Borden et al. (2012), and Kristensen and Martínez-Pañeda (2020) include the dynamic formulation with consideration of the inertial term of the rock momentum balance. Fracture branching is observed under dynamic formulation without fluid. Several authors have also presented numerical simulations using the phase-field method (Lee et al., 2016; Mikelić et al., 2015a; Mikelić et al., 2015b; Wheeler et al., 2020; J. Zhang & Yin, 2019; Zhou et al., 2019). In this study, our simulations are compared with laboratory experiments from Zhang et al. (2017) and Hou et al. (2017). In addition, simulations are conducted and compared with three simulations by different groups (Ha et al., 2018; Liu, Zhu, et al., 2018; A. Mikelić et al., 2015a). Our examples include fracturing by water, nitrogen, and CO_2.

Several authors have reported negative pressure in front of the fracture tip (A. Mikelić et al., 2015a; Salimzadeh & Khalili, 2015; Salimzadeh et al., 2017; Schrefler et al., 2006; Secchi & Schrefler, 2012). In Mikelić et al. (2015a), negative pressure is observed from the start of simulations and before fracture propagation. In Schrefler et al. (2006), Secchi & Schrefler, 2012, and Salimzadeh & Khalili, 2015, Salimzadeh et al. (2017), negative pressure is observed at the crack tip during fracture propagation. The authors reason that the fluid lag in filling the created fractures leads to negative pressure. In other words, a fluid speed that is lower than fracture propagation speed may result in negative pressure at the fracture tip. Detournay and Garagash (2003) investigate the fluid pressure at the tip of the cavity due to fluid lag. They state that fluid flow from surrounding pore space to the tip of cavity should result in a non-negative pressure. We suggest that the negative pressure from numerical simulations in the conventional finite element (FEM) is due to shortcomings of the method. Generally, the FE method may not describe fluid flow across the fracture boundaries correctly. In fact, the conventional finite element is not even locally mass conservative. In the past, negative pressure has been reported in an-isotropic porous media flow, even in the higher-order methods (Younes & Fontaine, 2008) from discretization. Because of potential effect of leak-off on fracture creation, the fluid flux calculation is a key focus in our work. In some models, a leak-off coefficient is introduced to adjust the leak-off between the fracture and the matrix (Liu, Qu, et al., 2018; Song et al., 2019). However, a clear interpretation of the selection of this coefficient for different fluids is missing. We use the mixed hybrid finite element, referred to as MFE method, to approximate pressure distribution in fractured media. This guarantees a continuous normal component of velocity field when passing from one element to the other (Chavent & Roberts, 1991). In our work, the implementation of the MFE method for incompressible flow is from Hoteit and Firoozabadi (2008) and for compressible flow is based on the work of Hoteit and Firoozabadi (2004) and Zidane and Firoozabadi (2014). The MFE method has been applied by Ha et al. (2018) in simulation of hydraulic fracturing without detailed formulation and analysis. In our work, we provide analysis and compare the results from MFE with the conventional FEM.

We implement the MFE method in pressure and phase-field calculation and examine the effect of the inertial term in momentum balance in fracturing based on the dynamic formulation. The critical energy release rate is obtained from experimental data of breakdown pressure of water, CO_2, and nitrogen fracturing fluids. The critical energy release rate is then used to predict fracture propagation and geometry of created fractures by the three fluids. Our work is in the 2D space. We start with a brief review of the theory, followed by a short discussion of numerical implementation. We compare our work with simulations from Mikelić et al. (2015a), Ha et al. (2018), and Liu, Zhu, et al. (2018), and laboratory measurements by Zhang et al. (2017) and Hou et al. (2017). We first predict pressure distribution from our MFE formulation at early pressurization stage and before breakdown and compare with simulations of Mikelić et al. (2015a) from FEM. Next, we examine the effect of dynamic formulation on pressure profile after breakdown and compare with simulations of Ha et al. (2018) of water and CO_2 fracturing. Later, we examine the contribution of dynamic formulation and boundary stress on fracture pattern in water and CO_2 fracturing, and compare our work with simulations of Liu, Zhu, et al. (2018) and the experimental work of Zhang et al. (2017) .We also simulate water and nitrogen fracturing and compare our work with laboratory measurements of Hou et al. (2017). Sensitivity to element size and regularization length (a parameter of the phase-field) is carried out in the two examples from laboratory measurements. This step is conducted to examine the effect of spatial discretization and to present converged simulation results.

2. Theory

The momentum balance and phase-field expression are obtained from the Euler-Lagrange equation of the variational formulation of Griffith's theory. In this formulation, fracture initiation at breakdown pressure and fracture propagation are based on minimization of the Lagrange energy functional. The momentum balance of the deformable rock is given by

$$\frac{\partial\left[\left(1-c\right)^2 \frac{\partial \psi_e^+}{\partial \varepsilon_{ij}} + \frac{\partial \psi_e^-}{\partial \varepsilon_{ij}}\right]}{\partial x_j} - \alpha_{eff}\frac{\partial p}{\partial x_j} + f_j = \rho \ddot{u}_j \quad \left(\text{dynamic formulation}\right) \tag{1a}$$

$$\frac{\partial\left[\left(1-c\right)^2 \frac{\partial \psi_e^+}{\partial \varepsilon_{ij}} + \frac{\partial \psi_e^-}{\partial \varepsilon_{ij}}\right]}{\partial x_j} - \alpha_{eff}\frac{\partial p}{\partial x_j} + f_j = 0 \quad \left(\text{quasi-static formulation}\right) \tag{1b}$$

where c is the phase-field variable; $\mathbf{x}$ is the location coordinate; $\mathbf{\varepsilon}$ is the strain tensor; $\mathbf{f}$ is the local load applied on the external boundary; bold fonts indicate vector or matrix; ψ_e^+ and ψ_e^- are the elastic strain energy density of positive and negative components of the strain tensor, respectively; α_{eff} is the effective Biot's coefficient; ρ is the mass density of the rock; i and j represent directions; i is a dummy index; and j is a free index.

We use FEM for discretization of displacements. For element K, the matrix notation of Equation 1 after discretization is given by

$$\mathbf{K}\mathbf{D}_K - \mathbf{Q}\mathbf{P}_K + \mathbf{M}\ddot{\mathbf{D}}_K = \mathbf{F} \quad \left(\text{dynamic formulation}\right) \tag{2a}$$

$$\mathbf{K}\mathbf{D}_K - \mathbf{Q}\mathbf{P}_K = \mathbf{F} \quad \left(\text{quasi-static formulation}\right) \tag{2b}$$

where $\mathbf{D}_K$, $\mathbf{P}_K$, and $\ddot{\mathbf{D}}_K$ are the nodal values for displacement, pressure, and acceleration fields, respectively; $\mathbf{F}$ is the external forces at the nodes; $\mathbf{K}$ is the stiffness matrix; $\mathbf{Q}$ is the poroelasticity matrix; and $\mathbf{M}$ is the mass matrix. The expressions for the variables in Equation 2 are given by Zienkiewicz (1982) which are presented in Text S1 of Supporting Information S1. Implicit direct integration method is used for dynamic formulation which is unconditionally stable (Kleiven et al., 2001). The domain is subdivided into three parts: rock, fracture, and transition domain. The displacement field is only calculated within rock and transition domains. Nodes inside the fracture domain are fixed.

The phase-field equation is given by

$$2(1-c)H - G_c \frac{c}{2l_0} + 2l_0 G_c \frac{\partial^2 c}{\partial x_i^2} = 0 \tag{3}$$

where G_c is the critical energy release rate, l_0 is the regularization length (defines the width of the smooth approximation at each side of the crack), and the H is strain-history field. An introduction to Griffith's theory and Equation 3 is presented in Text S2 of Supporting Information S1. The phase-field approximation of solid is presented in Text S3 of Supporting Information S1. The energy functional of fractured porous media and equations of motion are presented in Text S4 of Supporting Information S1.

We assume fluid flow in permeable media is described by Darcy's law. In the rock domain, the fluid mass balance is expressed as (Lee et al., 2016)

$$\rho_f \frac{\partial \left(\frac{1}{M} p + \alpha \varepsilon_{\mathrm{vol}} \right)}{\partial t} - \nabla \cdot \left(\rho_f \frac{k_R}{\mu_f} \nabla p \right) = Q \tag{4}$$

where p is fluid pressure, t is time, k_R is permeability of the rock, μ_f is fluid viscosity, ρ_f is fluid density, Q is the volumetric injection rate, $\varepsilon_{\mathrm{vol}}$ is the volumetric strain, and α is Biot's coefficient. The first term on the left describes the rate of fluid mass accumulation and the second term describes the mass rate of fluid flowing in and out of the domain. M is the Biot's modulus defined as

$$M = \frac{1}{C_s (\alpha - \phi)(1 - \alpha) + C_f \phi} \tag{5}$$

where C_s and C_f are the compressibility of the solid and fluid, respectively and ϕ is porosity.

Mass balance in the fracture domain leads to

$$\rho_f C_f \frac{\partial p}{\partial t} - \nabla \cdot \left(\rho_f \frac{k_F}{\mu_f} \nabla p \right) = Q \tag{6}$$

where k_F is the permeability of fracture.

In the transition domain, the fluid mass balance equation is expressed by

$$\rho_f C_{eff} \frac{\partial p}{\partial t} + \rho_f \alpha_{eff} \chi_R \frac{\partial \varepsilon_{\mathrm{vol}}}{\partial t} - \nabla \cdot \left(\rho_f \frac{k_{eff}}{\mu_f} \nabla p \right) = Q \tag{7}$$

where C_{eff} is the effective compressibility and k_{eff} is the effective permeability. The effective properties are calculated based on the mixing rule (Lee et al., 2016; Zhou et al., 2019) given below:

$$C_{eff} = C_s (\alpha_{eff} - \phi_{eff})(1 - \alpha_{eff}) + C_f \phi_{eff} \tag{8a}$$

$$k_{eff} = \chi_R k_R + \chi_F k_F \tag{8b}$$

$$\alpha_{eff} = \chi_R \alpha + \chi_F \tag{8c}$$

$$\phi_{eff} = \chi_R \phi + \chi_F \tag{8d}$$

where ϕ_{eff} is the effective porosity and χ_R and χ_F are the linear indicator functions of phase-field variable which vary between 0 and 1. In the transition region, the indicator functions are assumed to be related to the phase-field based on the following expressions:

$$\chi_R = \frac{c_2 - c}{c_2 - c_1}$$
$$\chi_F = \frac{c - c_1}{c_2 - c_1} \tag{9}$$

where c_1 and c_2 are two threshold values defining the boundaries of rock and fracture domains. Different authors use different values for c_1 and c_2. Zhou et al. (2019) assign $c_1 = 0.4$ or 0.5 and $c_2 = 1$. Lee et al. (2016) assign $c_1 = 0.4$ and $c_2 = 0.6$; we use the same values as Zhou et al.

The displacement, phase-field, and fluid pressure are solved from Equations 2, 3, and 7 in a staggered scheme. The displacement is calculated first, then the strain-history field is updated followed by the phase-field, and the fluid pressure is solved sequentially based on the updated results from the previous time step. The staggered scheme is readily implemented, but it may not be computationally as efficient as implicit approaches. Kristensen and Martínez-Pañeda (2020) implement a monolithic quasi-Newton scheme which is reported to be at least 10 times faster than the staggered scheme for fracturing simulation. There is no fluid flow in the implementation. As stated above, in our work we use the MFE for discretization of phase-field and pressure scalars and FEM for discretization of displacements. What we call the MFE is in fact the mixed hybrid finite element (MHFE), which is different from the conventional mixed finite element. It may not have been used before in simulation of flow in hydraulic fracturing. The formulation of MFE used in our simulations and its merits in accurate calculations of flow are presented in Text S5 of Supporting Information S1. We verify our implementation of the phase-field method with the analytical solution of fracture opening displacement of a pressurized fracture in static state by Sneddon and Lowengrub (1969) in Text S6 of Supporting Information S1.

3. Numerical Simulations

The focus of our work is on 2D unstructured discretization of equations describing hydraulic fracturing; unstructured triangle elements are used in all examples. The use of unstructured elements is motivated by fracture propagation in different directions. Recently we have observed that Fickian diffusion can be more accurately described by unstructured gridding (Zidane & Firoozabadi, 2021) due to the random nature of the process. The same may apply to fracture propagation. In this work, when we refer to element size, it is based on the average side length of a triangular element. We assume single phase flow and isothermal conditions and that the density, viscosity, and compressibility of water are constant. The density and compressibility of CO_2 and nitrogen are calculated based on the Peng-Robinson equation of state (Peng & Robinson, 1976). The viscosity of CO_2 and nitrogen are calculated from the Lohrenz-Bray-Clark model (Lohrenz et al., 1964). Simulations are conducted based on quasi-static formulation before breakdown with a larger time step and dynamic formulation after breakdown point with a smaller time step. Our numerical simulations are compared with simulations of early pressurization before fracture propagation by Mikelić et al. (2015a), fracture initiation and propagation from simulations by Ha et al. (2018) and Liu, Zhu, et al. (2018), and laboratory measurements by Zhang et al. (2017) and Hou et al. (2017) The simulations of laboratory experiments are presented in detail. One objective of laboratory simulations is to obtain the critical energy release rate for CO_2, water, and nitrogen fluids. This parameter is a key element of the phase-field, and to the best of our knowledge, previous simulations do not report the values for different fluids from laboratory testing.

3.1. Simulation of Pressure Field by the MFE and Comparison to the FEM

We have frequently observed negative pressure in fracture propagation when we used a commercial software based on the FEM. There are inherent advantages of MFE over FEM in numerical simulation of pressure field in fractured and in layered media (Hoteit & Firoozabadi, 2008; Zidane & Firoozabadi, 2014) as mentioned earlier. We compare pressure field in deformable fractured media from our MFE simulations to the simulations from Mikelić et al. (2015a) in the deal.II library. Figure 1a shows the dimension of domain and fracture, as well as boundary conditions. The sample size is 4×4 m. There is a fracture in the domain: fracture length is 0.4 m and fracture width is 0.18 m. The roller boundary condition is applied on all boundaries. Closed boundary condition (no fluid flow across boundaries) is assumed. The initial pressure throughout the domain is zero. The relevant parameters are listed in Table 1.

The compressibility of the solid C_s is calculated by

$$C_s = \frac{3(1 - 2\nu)}{E} \tag{10}$$
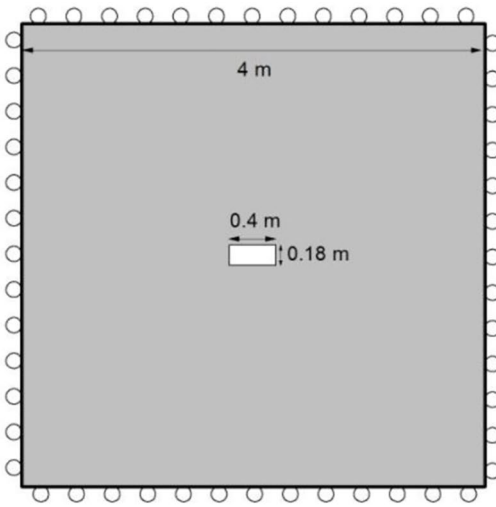
(a) Geometry and boundary conditions
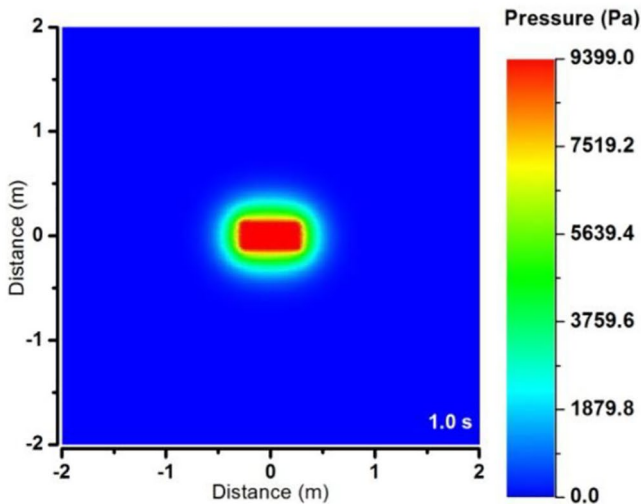
(b) MFE

Figure 1. (a) Geometry and boundary conditions of the simulations from Mikelić et al. (2015a), (b) Pressure profile simulated by MFE: time = 1 s after start of fluid injection.

Table 1
Parameters of Fluid Injection From Mikelić et al. (2015a)

E	10^8 Pa	N	0.2	G_c	1 N/m
l_0	88 mm	c_1	0.4	c_2	0.6
ϕ	0.01	ρ_f	1,000 kg/m³	α	1
k_R	10^{-8} mD	C_f	10^{-8} Pa^{-1}	Q	31.83 mm²/s
μ_f	0.001 Pa·s	Element size	2 cm		

and the fracture permeability k_F is calculated by

$$k_F = \frac{w^2}{12} \tag{11}$$

where E is the Young's modulus, ν is the Poisson's ratio, and w is the width of the fracture.

The work by Mikelić et al. (2015a) gives rise to negative pressure around the fracture in the deformable solid before fracture propagation. Our simulations based on MFE discretization do not give negative pressure (see Figure 1b).

3.2. Simulation of Hydraulic Fracturing by Water and by CO$_2$: Cement-Based Mortar Specimens

We carry out simulations for a cement-based mortar specimen based on dynamic formulation and compare results with Ha et al. (2018) in the deal.II library. The specimens have relatively high porosity and permeability. The geometry and boundary conditions are shown in Figure 2a. The domain is 1×1 m. The initial fracture length is 0.1 m and the width is 0.01 m. Boundary stress (8 MPa) is applied to top and right edges. The roller boundary condition is applied on left and bottom edges, with left-bottom corner fixed. Closed boundary condition is applied for fluid flow. Two simulations are conducted with water and CO$_2$ as injection fluids. The relevant parameters are listed in Table 2. The initial pressure is 8 MPa. An isothermal condition of 298.15 K is assumed. The inertial term is neglected in Ha et al. simulations (2018), and heterogeneity is assumed by assigning random fields for G_c and E generated by an exponential covariance model. In our work, we include the inertial term and the material is assumed to be homogeneous by assigning E as mean value of random field from Ha et al. (2018). G_c of CO$_2$ is also assumed to be mean value of random field from Ha et al. (2018). We determine G_c of water-rock by matching the breakdown pressure.

Figure 2b shows the pressure vs. time history in the notch. The breakdown pressure is lower in CO$_2$ fracturing. A sharp pressure drop is seen for water fracturing in our simulations while a gradual decrease is observed in Ha et al. (2018) The average propagation speed of fracture is 1.67 m/s in our simulations with dynamic formulation, 0.03 m/s with quasi-static formulation, and 0.014 m/s in Ha et al. simulations (2018). In fracture propagation, the inertial mass gives higher resistance to deceleration in the solid domain near the crack tip when responding to loading from the surrounding boundary. Figure 2c shows the effect of permeability of the rock and injection rate on breakdown pressure. When the permeability is low, there is less leak-off and larger increase of fluid pressure within the fracture, which leads to higher breakdown pressure (Li & Zhang, 2018). Similarly, when the injection rate is high, the increase in rate of fluid pressure within the fracture is also high, which results in a larger fracture volume under higher breakdown pressure.

Figures 2d and 2e shows the simulation results for phase-field distribution of water fracturing from our work. For a given time, the fracture is closer to the boundary in our simulations with dynamic formulation because the propagation speed is higher. Due to heterogeneity in material properties, the fracture propagates irregularly and mainly downward in
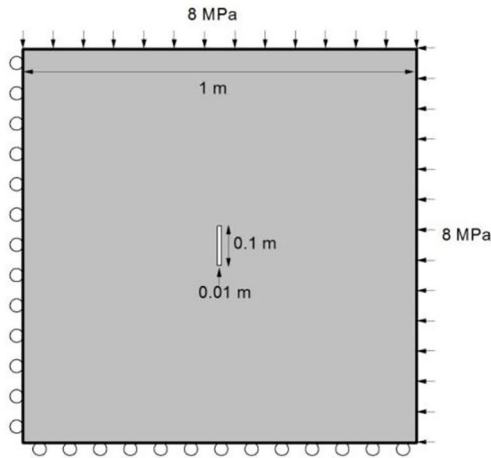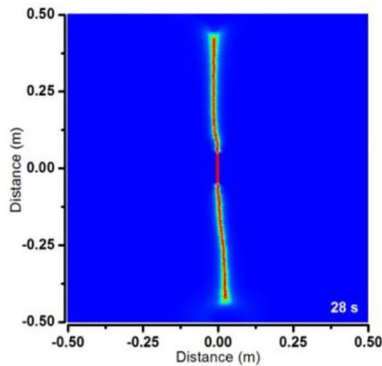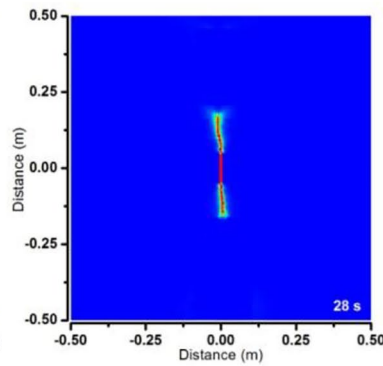
(a) Geometry and boundary conditions
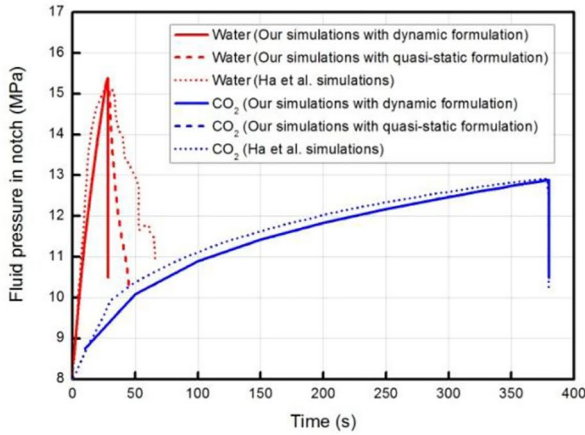
(b) Pressure vs. time in the notch: water and CO_2 fracturing
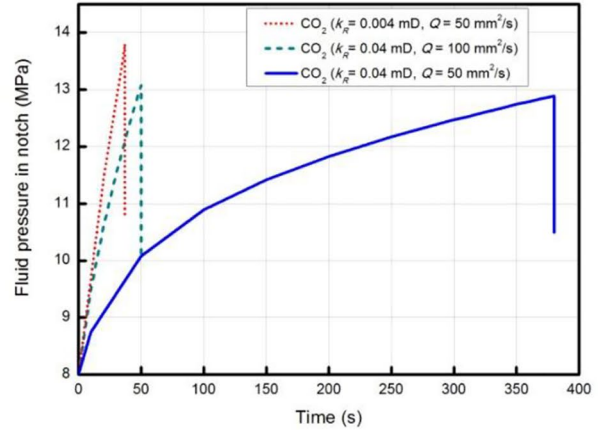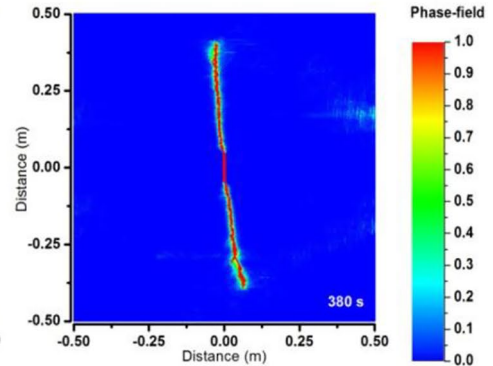

(c) Pressure vs. time in the notch: sensitivity to k_R and Q

(d) Water fracturing: dynamic formulation

(e) Water fracturing: quasi-static formulation

(f) CO_2 fracturing: dynamic formulation

Figure 2.

Table 2
Relevant Parameters in Simulations of Ha et al. (2018) (G_c of Water Is Not Provided by Ha et al. (2018); It Is Obtained by Matching Breakdown Pressure)

E	25 GPa	N	0.3	G_c	50 N/m (CO_2) 370 N/m (water)
l_0	12 mm	c_1	0.4	c_2	0.6
ϕ	0.2	ρ_f (Water)	1,000 kg/m³	α	0.2
k_R	0.04 mD	C_f (Water)	4.6×10^{-10} Pa^{-1}	Q	50 mm²/s
μ_f (Water)	8.9×10^{-4} Pa·s	Element size	5 mm		

simulations from Ha et al. (2018); in our work, the fracture path propagates in both directions. Figure 2f shows phase-field distribution in CO_2 fracturing from our simulations. A similar fracture path for propagation is observed in both directions. The spreading of phase-field in simulations by Ha et al. (2018) is high and not reported by other authors. Sensitivity analysis to element size in our work shows no appreciable effect on the results.

3.3. Simulations of Hydraulic Fracturing by Water and by CO_2 and Comparison With Experiments: Shale Specimens

Our simulations based on dynamic formulation are compared with simulations by Liu, Zhu, et al. (2018) in COMSOL and experiments from Zhang et al. (2017) in shale, which has low porosity and permeability. Shale samples are from outcrops of the Lower Silurian Longmaxi formation in the Sichuan basin, China. Shale mineralogy is about 3.8% plagioclase, 11.7% calcite, 40.2% quartz, and 15.1% clay minerals, belonging to brittle rock. Damage evolution law is used in the simulations by Liu, Zhu, et al. (2018). The geometry is shown in Figure 3a. The sample size is 200 × 200 mm. The initial fracture is circular with a diameter of 15 mm. Triaxial loading is applied in the experiments by Zhang et al. (2017) with a vertical stress of 12 MPa and two horizontal stresses σ_H (10 MPa) and σ_h (8 MPa). Only horizontal stresses are considered in our 2D simulations. The roller boundary condition is applied on remaining edges, with one corner fixed. Closed boundary condition with no flow is applied for pressure in line with experimental setup. Two simulations are conducted for fracturing by water and CO_2. The relevant parameters are listed in Table 3. Q is based on injection rate (30 ml/min) and length of hole (20 mm) from the experiments by Zhang et al. (2017). The initial pressure is 1 atm for water fracturing and 6 MPa for CO_2 fracturing. Specimens are heated at 333.15 K for 24 h before experiments, and an isothermal condition at the same temperature is assumed in our simulations.
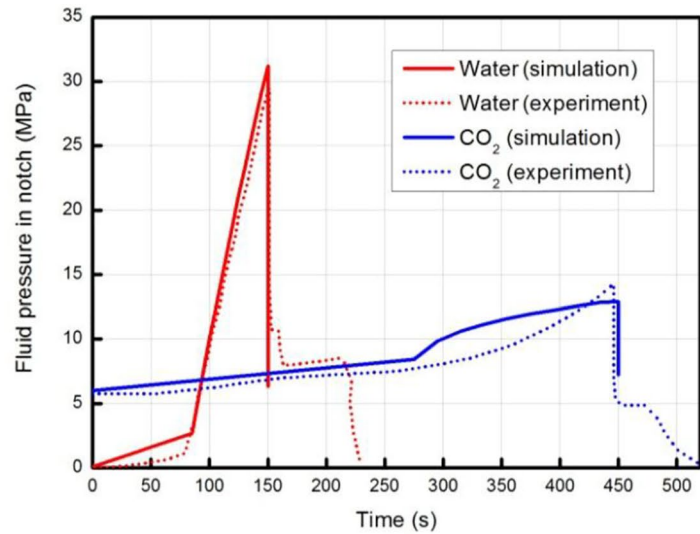
Figure 3b shows pressure vs. time at the fracture center. Similar to Figure 2b, the breakdown pressure is lower in CO_2 fracturing. A sharp drop is seen in the experiment, which further confirms the significant effect of the inertial term in fracturing based on dynamic formulation.

Figures 4a–4d shows the fracture pattern in water fracturing from experiments by Zhang et al. (2017), simulations by Liu, Zhu, et al. (2018), and our phase-field simulations in water fracturing at time = 150 s. The time is not specified in Liu, Zhu, et al. (2018). A single vertical fracture is observed in both simulations. The effect of inertial term is not significant because G_c is high. Figures 4e–4h depicts the fracture pattern in CO_2 from simulations and experiments at time = 450 s. The time is not reported by Liu, Zhu, et al. (2018). Both simulations show two main fractures propagating simultaneously, which confirm that CO_2 induced fractures may have more complex geometry than water-induced fractures. Our simulations based on quasi-static formulation shown in Figure 4h give one fracture. Multiple fracture branching may be observed from simulations under dynamic formulation depending on the value of G_c.

Figure 2. (a) Geometry and boundary conditions of the setup from Ha et al. (2018); (b) Pressure in the notch vs. time in water and CO_2 fracturing. Solid lines represent our simulations and dotted lines represent simulations by Ha et al. (2018); (c) Pressure in the notch vs. time in CO_2 fracturing from different permeability and injection rates; (d–e) Phase-field distribution from water fracturing, and (f) CO_2 fracturing. The pressure profile in (b and c) refers to the complete process until the fracture reaches the boundary, while the phase-field distribution presented in (d and f) is before the fracture propagates to the boundary to compare our results with Ha et al. (2018).
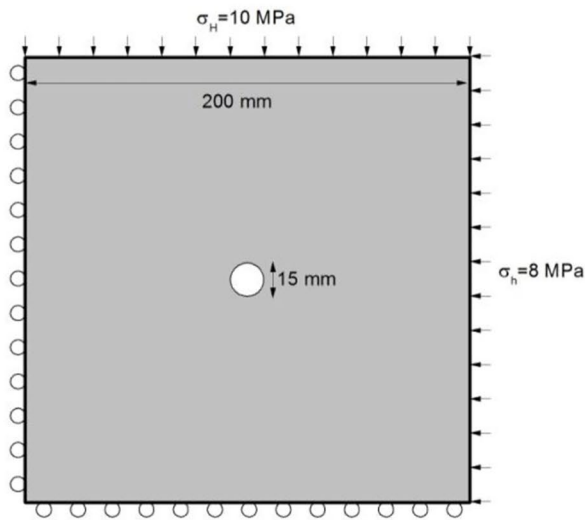
(a) Geometry and boundary conditions

(b) Pressure vs. time in the notch

Figure 3. (a) Geometry and boundary conditions of the setup from Liu, Zhu, et al. (2018); (b) Comparison between pressure vs. time at the injection domain in water and CO2 fracturing–solid lines are from our simulations, dotted lines represent experimental measurements by Zhang et al. (2017) The pressure profile in (b) refers to the complete process until the fracture reaches the boundary.

The effect of horizontal stress difference in CO_2 fracturing from our simulations is compared to experiments by Zhang et al. (2017). Five simulations are performed with stress differences of 0 ($\sigma_H = \sigma_h = 10$ MPa), 1 ($\sigma_H = 9$ MPa, $\sigma_h = 8$ MPa), 2 ($\sigma_H = 10$ MPa, $\sigma_h = 8$ MPa), 3 ($\sigma_H = 9$ MPa, $\sigma_h = 6$ MPa), and 4 MPa ($\sigma_H = 10$ MPa, $\sigma_h = 6$ MPa). The fracture patterns from experiments by Zhang et al. (2017) and our phase-field simulations are presented in Figure 5. When the stress difference is small, the fractures are evenly distributed around the hole and propagations are in all directions with significant branching. When the stress difference is large, a single main crack is formed along the direction of maximum horizontal stress, with less branching. Although the small branches observed in experiments are not reproduced in our simulation as the vertical stress and natural fractures are not considered, the trend is clearly captured. The predicted breakdown pressure is affected by σ_H-σ_h. The breakdown pressures are about 15.7, 13.6, 12.9, 10.4, and 10.1 MPa, with stress differences of 0, 1, 2, 3, and 4 MPa, respectively. We also perform simulations for a large stress difference of 10 MPa ($\sigma_H = 16$ MPa, $\sigma_h = 6$ MPa) to examine the effect on fracturing. For this case, fractures are initiated at two different locations instantaneously. Simulation results are presented in the Text S7 of Supporting Information S1.

We have conducted sensitivity analysis to element size and regularization length in our simulations for some of the measurements by Zhang et al. (2017) of CO_2 fracturing. When $\sigma_H-\sigma_h = 0$ MPa, multiple branches are simulated in three different element sizes as shown in Figures 6a–6c. When σ_H-$\sigma_h = 4$ MPa, a bi-wing fracture is simulated in three different element sizes as shown in Figures 6g–6i. Although the detailed fracture patterns are different, the trends from our simulations showing effect of stress difference are consistent with experiments. The simulated fracture patterns are similar for different values of l_0 as shown in Figures 6d–6f

Table 3

Parameters for Simulation of Liu, Zhu, et al. (2018) and Zhang et al. (2017) (We Obtain G_c by Matching the Breakdown Pressure)

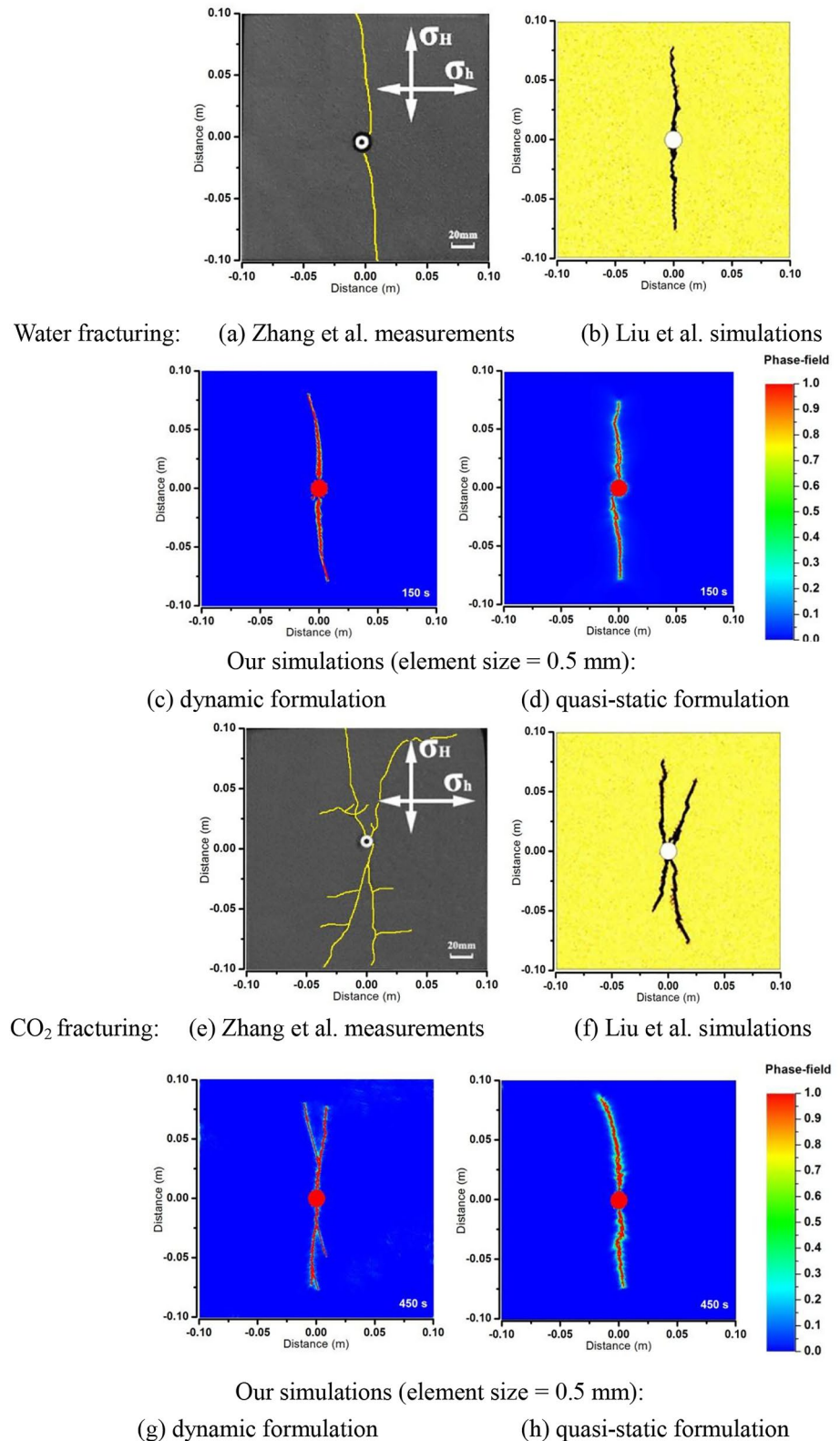| E	33 GPa	N	0.35	G_c	10 N/m (CO_2-shale) 130 N/m (water-shale)
l_0	1 mm	c_1	0.4	c_2	0.6
ϕ	0.01	ρ_f (Water)	1,000 kg/m^3	α	0.01
k_R	0.001 mD	C_f (Water)	4.6×10^{-10} Pa^{-1}	Q	25 mm^2/s
μ_f (Water)	4.688×10^{-4} Pa·s	Element size	0.5 mm		

Figure 4. (a–d) Fracture pattern for water fracturing; (e–h) Fracture pattern for CO_2 fracturing. The phase-field distribution presented in (c, d) and (g, h) is before fractures propagating to the boundary to match the results of Liu, Zhu, et al. (2018), (a and e) are adapted from Zhang et al. (2017), (b and f) are adapted from Liu, Zhu, et al. (2018), with permission from Elsevier.
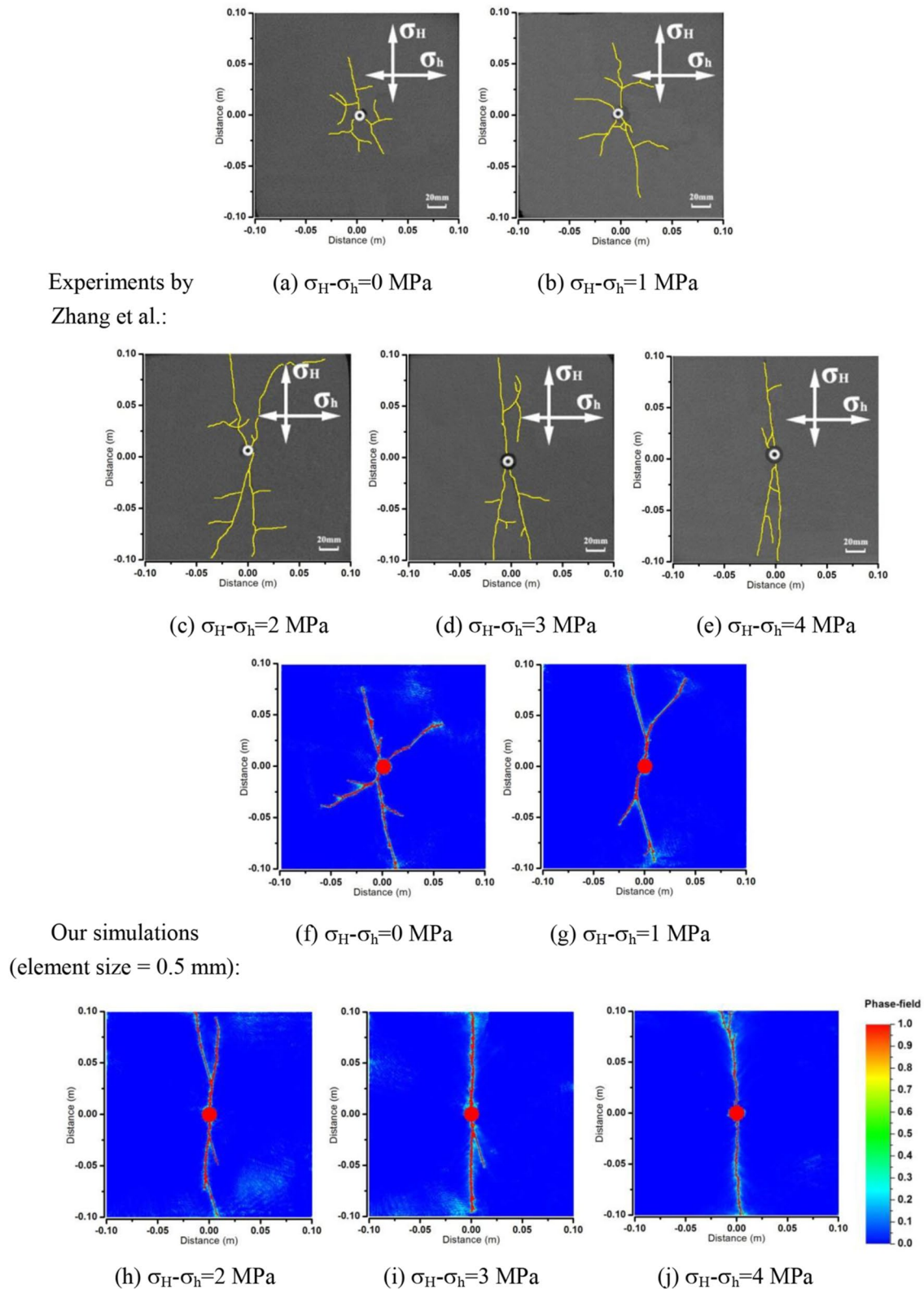
Figure 5. Fracture pattern in CO_2 fracturing at five stress differences: (a–e) experiments by Zhang et al. (2017) and (f–j) our simulations of phase-field distributions by dynamic formulation. (a–e) are adapted from (X. Zhang et al., 2017), with permission from Elsevier.
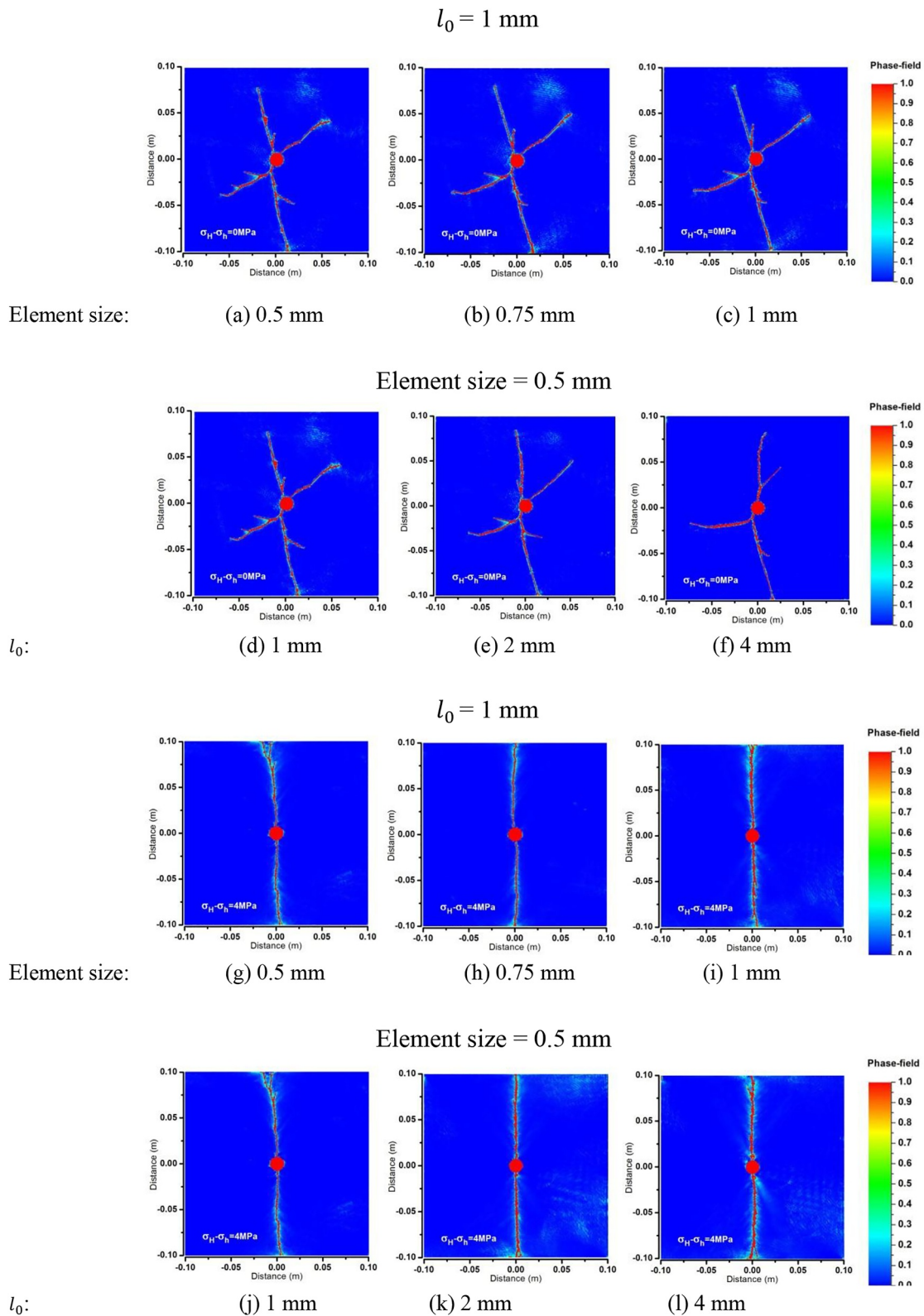
Figure 6. Effect of element size and regularization length on simulated phase-field distribution for CO_2 fracturing in shale: (a–c) element size, stress difference = 0; (d–f) regularization length l_0, stress difference = 0; (g–i) element size, stress difference = 4 MPa; (j–l) regularization length l_0, stress difference = 4 MPa.
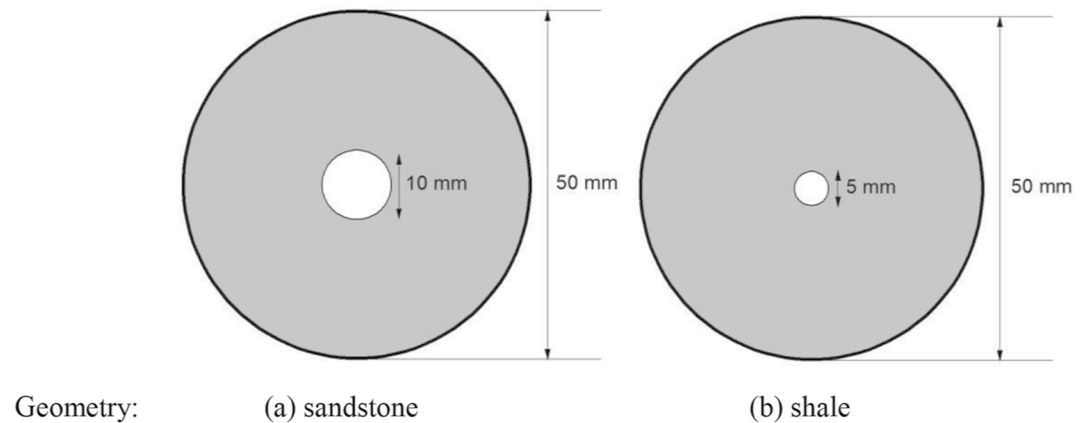
Figure 7. Geometry of the experimental setup from Hou et al. (2017) for (a) sandstone, and (b) shale.

and 6j–6l. In our work, l_0 is assigned a value equal or larger than fracture width; there is no significant effect on fracture pattern in the range of 1–2 mm. Kristensen et al. (2021) and Tanné et al. (2018) have suggested that l_0 can be estimated based on material strength and fracture toughness. Materials with lower strength or higher fracture toughness have a higher l_0. The suggestion of the authors will be considered in future work. The fluid pressure, displacements, and stresses corresponding to Figures 6d–6f and 6j–6l) are shown in Text S8 of Supporting Information S1. We also examine the fracture width in simulations, when fracking fluid injection is stopped at the time of breakdown pressure, and when Young's modulus is considered to change from heterogeneity. The results are presented in Text S9 of Supporting Information S1. The effect of fluid injection halt on fracture propagation is observed in mildly less branching in CO_2 fracking. The work on injection fluid halt will be further investigated in large domains in the future. The heterogeneity in Young's modulus affects branching, but not significantly.

3.4. Simulations of Hydraulic Fracturing by Water and by Nitrogen and Comparison With Experiments: Sandstone and Shale Specimens

Water and nitrogen fracturing based on dynamic formulation are simulated and compared with experimental data from Hou et al. (2017) in sandstone and shale rocks. Red sandstone with a relatively homogeneous pore structure is from a mine in Xuzhou City, Jiangsu Province, China. The shale samples are from outcrops of the Longmaxi formation in Shizhu County of Chongqing City, China. The rock samples have a cylindrical shape with 100 mm length and 50 mm diameter. A borehole with 60 mm length is drilled axially with 10 mm diameter in the sandstone sample and 5 mm diameter in the shale sample. Fracturing fluid is injected into the borehole at a constant pressurization rate. A uniaxial stress of 4 MPa is applied in the experiments but is not considered in our work because of 2D formulation. Other directions are unconfined. Because of the high length-to-diameter ratio, a 2D simulation may capture the essence of experiments. The fracture pattern at the end face is simulated with the geometry for the sandstone sample in Figure 7a and shale sample in Figure 7b. Open boundary condition is applied for pressure field. Four simulations are conducted for water and nitrogen as fracturing fluids. The parameters used in simulations are listed in Table 4. The initial pressure is 1 atm and the temperature is 298.15 K.

Hou et al. (2017) measure a lower breakdown pressure for nitrogen than water, and sandstone has a lower breakdown pressure than shale. We determine the critical energy release rate G_c based on measured breakdown pressure. Nitrogen fracturing of sandstone has lower G_c, while water fracturing in shale has the highest G_c as listed in Table 4. The breakdown pressure from our simulations is 3.1 MPa for water-sandstone, 2.45 MPa for nitrogen-sandstone, 10.8 MPa for water-shale, and 6.1 MPa for nitrogen-shale. The simulated fracture patterns are shown in Figure 8. A bi-wing fracture is observed in sandstone for both fracturing fluids, but the nitrogen-induced fracture is more tortuous (Figure 8e) with increased fracture surface area

Table 4
Parameters for Simulation of Experiments by Hou et al. ([2017](#)) (G_c Is Obtained by Matching Breakdown Pressure)

E	18.09 GPa (Sandstone) 13.98 GPa (Shale)	ν	0.31 (Sandstone) 0.33 (Shale)	G_c	40 N/m (Water-Sandstone) 15 N/m (Nitrogen-sandstone) 130 N/m (Water-shale) 25 N/m (Nitrogen-shale)
l_0	1 mm	c_1	0.4	c_2	0.6
ϕ	0.0818 (Sandstone) 0.0155 (Shale)	ρ_f (Water)	1,000 kg/m^3	α	0.0818 (Sandstone) 0.0155 (Shale)
k_R	0.1084 mD (Sandstone) 6.454×10^{-5} mD (Shale)	C_f (Water)	4.6×10^{-10} Pa^{-1}	Pressurization rate	0.0075 MPa/s (Water-sandstone) 0.075 MPa/s (Nitrogen-sandstone) 0.029 MPa/s (Water-shale) 0.015 MPa/s (Nitrogen-shale)
μ_f (Water)	8.9×10^{-4} Pa·s	Element size	0.25 mm		

and more penetration into the rock (Hou et al., [2017](#)). For shale, a bi-wing fracture is observed for water fracturing (Figure [8h](#)), and multiple branches are observed for nitrogen fracturing. Simulations are also conducted under quasi-static formulation (Figures [8c, 8f, 8i](#), and [8l](#)). The simulation results from dynamic and quasi-formulation are about the same due to high G_c. Our simulated fracture patterns are in good agreement with experimental data by Hou et al. ([2017](#)).

We conduct sensitivity analysis in element size and regularization length in simulations of phase-field distribution for nitrogen fracturing in shale. As shown in Figures [9a–9c](#), a similar fracture pattern is simulated with three different element sizes. The simulated fracture patterns are also similar for three different values of l_0 as shown in Figures [9d–9f](#).

4. Conclusions

The following have been partly reported in the literature; we reconfirm them fully:

1. Fracturing by water has higher breakdown pressure than by CO_2 and nitrogen. The fractures induced by CO_2 and nitrogen are more likely to have branching and complex patterns compared to water. The fracture surface area by CO_2 is the highest, followed by nitrogen; water has the lowest fracture surface area.
2. The critical energy release rate G_c of water-shale is higher than nitrogen-shale and CO_2-shale. Higher G_c leads to higher breakdown pressure and lower G_c may lead to branching.

The new findings from our work are:

Breakdown pressure can be used to determine accurately the critical energy release rate of a fluid-rock system in the phase field.

1. The implementation of the mixed hybrid finite element method improves the accuracy of pressure simulations and resolves the negative pressure simulations in the conventional finite element method when there are sharp changes in pressure from fracture to matrix.
2. The inertial term in the momentum balance equation of deformable media may have a significant effect on fracture propagation and branching. Multiple fracture branching may be observed when the inertial term is included in the momentum balance equation. The effect of dynamic formulation on simulations may not be significant when G_c is high.

The work has set the stage for adaptive gridding around the fractures and extension to 3D now that we have advanced accurate pressure calculation from the MFE method. In future, we plan to incorporate thermoelasticity to simulate the effect of temperature change for cold fluid injection in hot formations or where a fluid such as CO_2 may undergo temperature change due to significant pressure drop. We also plan to expand into a number of topics including use of a different G_c (from initial fracturing) in part of the fracture surface which is not exposed to injection fluid, and large-scale applications.
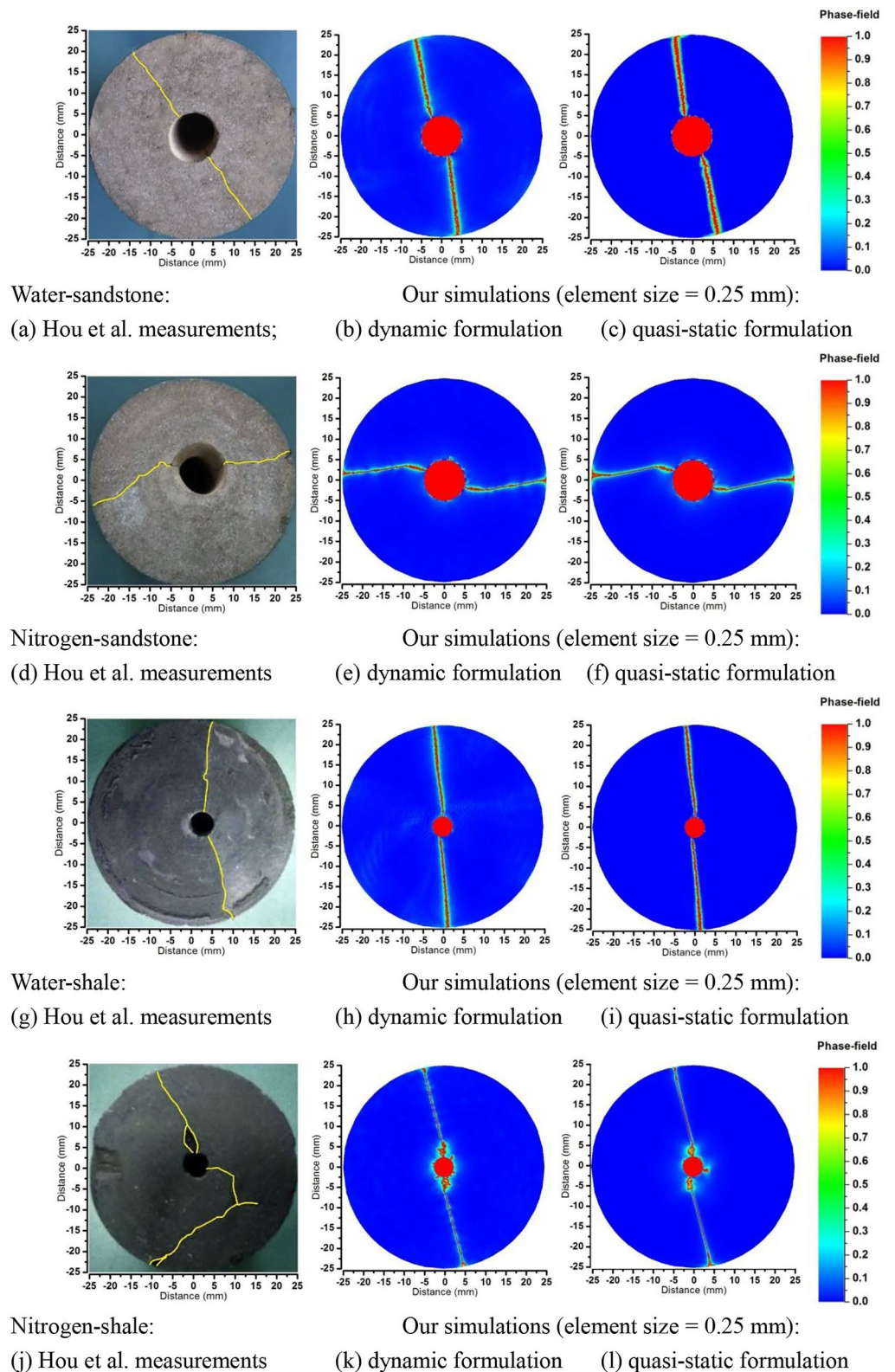
Figure 8. Fracture pattern for (a–c) water fracturing in sandstone; (d–f) nitrogen fracturing in sandstone; (g–i) water fracturing in shale; (j–l) nitrogen fracturing in shale. (a, d, g, and j) are adapted from (Hou et al., 2017), with permission from Elsevier.
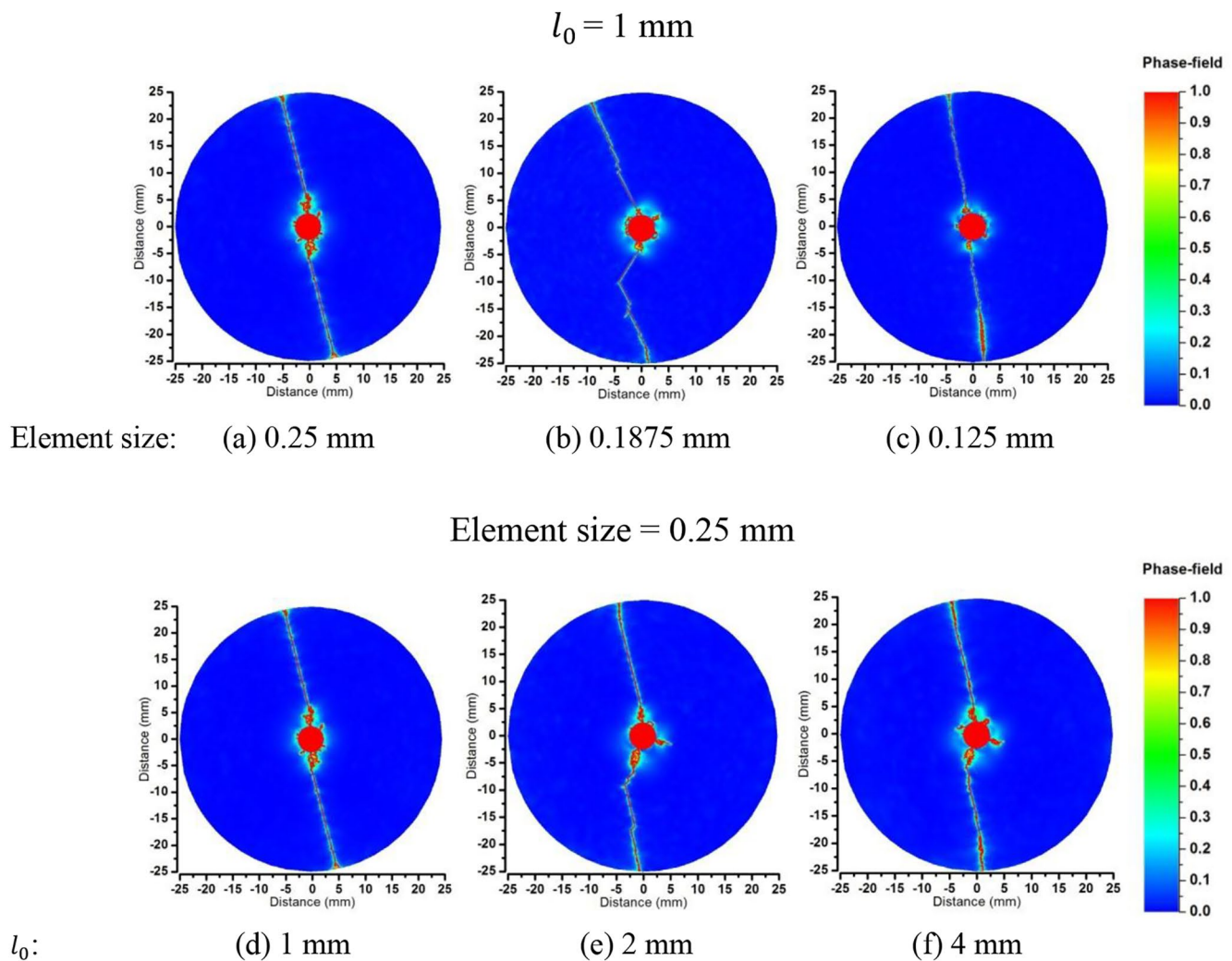
$$l_0 = 1 \text{ mm}$$

Figure 9. Sensitivity analysis on simulations of phase-field distribution for nitrogen fracturing in shale (a–c) element size; (d–f) regularization length l_0.

Data Availability Statement

Data files of simulations are available on the Open Science Framework at https://osf.io/d4zsy/quickfiles.

References

Alpak, F. O. (2021). A cohesive-zone model for simulating hydraulic-fracture evolution within a fully coupled flow/geomechanics-simulation System. *SPE Journal*, *26*(01), 22–43. https://doi.org/10.2118/193825-PA%JSPEJournal

Borden, M. J., Verhoosel, C. V., Scott, M. A., Hughes, T. J. R., & Landis, C. M. (2012). A phase-field description of dynamic brittle fracture. *Computer Methods in Applied Mechanics and Engineering*, *217–220*, 77–95. https://doi.org/10.1016/j.cma.2012.01.008

Carrier, B., & Granet, S. (2012). Numerical modeling of hydraulic fracture problem in permeable medium using cohesive zone model. *Engineering Fracture Mechanics*, *79*, 312–328. https://doi.org/10.1016/j.engfracmech.2011.11.012

Chavent, G., & Roberts, J. E. (1991). A unified physical presentation of mixed, mixed-hybrid finite elements and standard finite difference approximations for the determination of velocities in waterflow problems. *Advances in Water Resources*, *14*(6), 329–348. https://doi.org/10.1016/0309-1708(91)90020-O

Chen, Z., Bunger, A. P., Zhang, X., & Jeffrey, R. G. (2009). Cohesive zone finite element-based modeling of hydraulic fractures. *Acta Mechanica Solida Sinica*, *22*(5), 443–452. https://doi.org/10.1016/S0894-9166(09)60295-0

Dean, R. H., & Schmidt, J. H. (2009). Hydraulic-fracture predictions with a fully coupled geomechanical reservoir simulator. *SPE Journal*, *14*(04), 707–714. https://doi.org/10.2118/116470-PA%JSPEJournal

Detournay, E., & Garagash, D. I. (2003). The near-tip region of a fluid-driven fracture propagating in a permeable elastic solid. *Journal of Fluid Mechanics*, *494*, 1–32. https://doi.org/10.1017/s0022112003005275

Griffith, A. A. (1921). VI. The phenomena of rupture and flow in solids. *The Phenomena of Rupture and Flow in Solids*, *221*, 163–198. https://doi.org/10.1098/rsta.1921.0006

Ha, S. J., Choo, J., & Yun, T. S. (2018). Liquid CO_2 fracturing: Effect of fluid permeation on the breakdown pressure and cracking behavior. *Rock Mechanics and Rock Engineering*, *51*(11), 3407–3420. https://doi.org/10.1007/s00603-018-1542-x

Hillerborg, A., Modéer, M., & Petersson, P. E. (1976). Analysis of crack formation and crack growth in concrete by means of fracture mechanics and finite elements. *Cement and Concrete Research*, *6*(6), 773–781. https://doi.org/10.1016/0008-8846(76)90007-7

Hoteit, H., & Firoozabadi, A. (2004). *Compositional modeling by the combined discontinuous galerkin and mixed methods*. Paper presented at the SPE Annual Technical Conference and Exhibition.

Hoteit, H., & Firoozabadi, A. (2008). An efficient numerical model for incompressible two-phase flow in fractured media. *Advances in Water Resources*, *31*(6), 891–905. https://doi.org/10.1016/j.advwatres.2008.02.004

Hou, P., Gao, F., Ju, Y., Yang, Y., Gao, Y., & Liu, J. (2017). Effect of water and nitrogen fracturing fluids on initiation and extension of fracture in hydraulic fracturing of porous rock. *Journal of Natural Gas Science and Engineering*, *45*, 38–52. https://doi.org/10.1016/j.jngse.2017.05.012

Kleiven, S., Halldin, P., & Zenkert, D. (2001). Dynamic Finite Element Methods - Lecture Notes for SD2450 Biomechanics and Neuronics.

Kristensen, P. K., & Martínez-Pañeda, E. (2020). Phase field fracture modelling using quasi-Newton methods and a new adaptive step scheme. *Theoretical and Applied Fracture Mechanics*, *107*, 102446. https://doi.org/10.1016/j.tafmec.2019.102446

Kristensen, P. K., Niordson, C. F., & Martinez-Paneda, E. (2021). An assessment of phase field fracture: Crack initiation and growth. *Philos Trans A Math Phys Eng Sci*, *379*(2203), 20210021. https://doi.org/10.1098/rsta.2021.0021

Lee, S., Wheeler, M. F., & Wick, T. (2016). Pressure and fluid-driven fracture propagation in porous media using an adaptive finite element phase field model. *Computer Methods in Applied Mechanics and Engineering*, *305*, 111–132. https://doi.org/10.1016/j.cma.2016.02.037

Li, S., Firoozabadi, A., & Zhang, D. (2020). Hydromechanical modeling of nonplanar three-dimensional fracture propagation using an iteratively coupled approach. *Journal of Geophysical Research: Solid Earth*, *125*(8). https://doi.org/10.1029/2020jb020115

Li, S., & Zhang, D. (2018). How Effective Is Carbon Dioxide as an Alternative Fracturing Fluid?. *SPE Journal*, *24*(02), 857–876. https://doi.org/10.2118/194198-PA%JSPEJournal

Liu, L., Zhu, W., Wei, C., Elsworth, D., & Wang, J. (2018a). Microcrack-based geomechanical modeling of rock-gas interaction during supercritical CO2 fracturing. *Journal of Petroleum Science and Engineering*, *164*, 91–102. https://doi.org/10.1016/j.petrol.2018.01.049

Liu, X., Qu, Z., Guo, T., Wang, D., Tian, Q., & Lv, W. (2018b). A new chart of hydraulic fracture height prediction based on fluid-solid coupling equations and rock fracture mechanics. *R Soc Open Sci*, *5*(10), 180600. https://doi.org/10.1098/rsos.180600

Lohrenz, J., Bray, B. G., & Clark, C. R. (1964). Calculating Viscosities of Reservoir Fluids From Their Compositionsof Petroleum Technology. *Journal of Petroleum Technology*, *16*(10), 1171–1176. https://doi.org/10.2118/915-PA%JJournal

Middleton, R. S., Carey, J. W., Currier, R. P., Hyman, J. D., Kang, Q., Karra, S., et al. (2015). Shale gas and non-aqueous fracturing fluids: Opportunities and challenges for supercritical CO2. *Applied Energy*, *147*, 500–509. https://doi.org/10.1016/j.apenergy.2015.03.023

Miehe, C., Hofacker, M., & Welschinger, F. (2010). A phase field model for rate-independent crack propagation: Robust algorithmic implementation based on operator splits. *Computer Methods in Applied Mechanics and Engineering*, *199*(45–48), 2765–2778. https://doi.org/10.1016/j.cma.2010.04.011

Mikelić, A., Wheeler, M. F., & Wick, T. (2015a). Phase-field modeling of a fluid-driven fracture in a poroelastic medium. *Computational Geosciences*, *19*(6), 1171–1195. https://doi.org/10.1007/s10596-015-9532-5

Mikelić, A., Wheeler, M. F., & Wick, T. (2015b). A quasi-static phase-field approach to pressurized fractures. *Nonlinearity*, *28*(5), 1371–1399. https://doi.org/10.1088/0951-7715/28/5/1371

Ortiz, M., & Pandolfi, A. (1999). Finite-deformation irreversible cohesive elements for three-dimensional crack-propagation analysis. *CO*, *44*(9), 12672–12827. https://doi.org/10.1002/(SICI)1097-0207(19990330)44:9<1267::AID-NME486>3.0

Peng, D.-Y., & Robinson, D. B. (1976). A new two-constant equation of state. *Industrial & Engineering Chemistry Fundamentals*, *15*(1), 59–64. https://doi.org/10.1021/i160057a011

Salimzadeh, S., & Khalili, N. (2015). A three-phase XFEM model for hydraulic fracturing with cohesive crack propagation. *Computers and Geotechnics*, *69*, 82–92. https://doi.org/10.1016/j.compgeo.2015.05.001

Salimzadeh, S., Paluszny, A., & Zimmerman, R. W. (2017). Three-dimensional poroelastic effects during hydraulic fracturing in permeable rocks. *International Journal of Solids and Structures*, *108*, 153–163. https://doi.org/10.1016/j.ijsolstr.2016.12.008

Schrefler, B. A., Secchi, S., & Simoni, L. (2006). On adaptive refinement techniques in multi-field problems including cohesive fracture. *Computer Methods in Applied Mechanics and Engineering*, *195*(4–6), 444–461. https://doi.org/10.1016/j.cma.2004.10.014

Secchi, S., & Schrefler, B. A. (2012). A method for 3-D hydraulic fracturing simulation. *International Journal of Fracture*, *178*(1–2), 245–258. https://doi.org/10.1007/s10704-012-9742-y

Sneddon, I. N., & Lowengrub, M. (1969). *Crack problems in the classical theory of elasticity*. Wiley.

Song, X., Guo, Y., Zhang, J., Sun, N., Shen, G., Chang, X., et al. (2019). Fracturing with carbon dioxide: From microscopic mechanism to reservoir application. *Joule*, *3*(8), 1913–1926. https://doi.org/10.1016/j.joule.2019.05.004

Steinke, C., Zreid, I., & Kaliske, M. (2016). On the relation between phase-field crack approximation and gradient damage modelling. *Computational Mechanics*, *59*(5), 717–735. https://doi.org/10.1007/s00466-016-1369-9

Tanné, E., Li, T., Bourdin, B., Marigo, J. J., & Maurini, C. (2018). Crack nucleation in variational phase-field models of brittle fracture. *Journal of the Mechanics and Physics of Solids*, *110*, 80–99. https://doi.org/10.1016/j.jmps.2017.09.006

Thomas, L., Tang, H., Kalyon, D. M., Aktas, S., Arthur, J. D., Blotevogel, J., et al. (2019). Toward better hydraulic fracturing fluids and their application in energy production: A review of sustainable technologies and reduction of potential environmental impacts. *Journal of Petroleum Science and Engineering*, *173*, 793–803. https://doi.org/10.1016/j.petrol.2018.09.056

Urban-Rascon, E., & Aguilera, R. (2020). *Hydraulic fracturing modeling, fracture network, and microseismic monitoring*. Paper presented at the SPE Canada Unconventional Resources Conference.

van Dam, D. B., Papanastasiou, P., & de Pater, C. J. (2002). Impact of rock plasticity on hydraulic fracture propagation and closure SPE production & facilities. *SPE Production & Facilities*, *17*(03), 149–159. https://doi.org/10.2118/78812-PA%J

Wang, J., Elsworth, D., Wu, Y., Liu, J., Zhu, W., & Liu, Y. (2017). The Influence of Fracturing Fluids on Fracturing Processes: A Comparison Between Water, Oil and SC-CO2. *Rock Mechanics and Rock Engineering*, *51*(1), 299–313. https://doi.org/10.1007/s00603-017-1326-8

Wang, J. G., & Zhang, X. X. (2018). Fracturing behavior of shale reservoirs in water, N2 and SC-CO2 fracturing process. In (pp. 207–215). https://doi.org/10.1201/9781351042666-21

Wheeler, M. F., Wick, T., & Lee, S. (2020). IPACS: Integrated Phase-Field Advanced Crack Propagation Simulator. An adaptive, parallel, physics-based-discretization phase-field framework for fracture propagation in porous media. *Computer Methods in Applied Mechanics and Engineering*, *367*, 113124. https://doi.org/10.1016/j.cma.2020.113124

Wu, T., & Firoozabadi, A. (2021). Calculation of solid–fluid interfacial free energy with consideration of solid deformation by molecular dynamics simulations. *The Journal of Physical Chemistry A*, *125*(26), 5841–5848. https://doi.org/10.1021/acs.jpca.1c00735

Younes, A., & Fontaine, V. (2008). Efficiency of mixed hybrid finite element and multipoint flux approximation methods on quadrangular grids and highly anisotropic media. *International Journal for Numerical Methods in Engineering*, *76*(3), 314–336. https://doi.org/10.1002/nme.2327

Zhang, J., & Yin, S. (2019). A three-dimensional solution of hydraulic fracture width for wellbore strengthening applications. *Petroleum Science*, *16*(4), 808–815. https://doi.org/10.1007/s12182-019-0317-7

Zhang, Q., Ma, D., Liu, J., Wang, J., Li, X., & Zhou, Z. (2019). Numerical simulations of fracture propagation in jointed shale reservoirs under CO_2 fracturing. *Geofluids*, *2019*, 1–13. https://doi.org/10.1155/2019/2624716

Zhang, X., Lu, Y., Tang, J., Zhou, Z., & Liao, Y. (2017). Experimental study on fracture initiation and propagation in shale using supercritical carbon dioxide fracturing. *Fuel*, *190*, 370–378. https://doi.org/10.1016/j.fuel.2016.10.120

Zhou, S., Zhuang, X., & Rabczuk, T. (2019). Phase-field modeling of fluid-driven dynamic cracking in porous media. *Computer Methods in Applied Mechanics and Engineering*, *350*, 169–198. https://doi.org/10.1016/j.cma.2019.03.001

Zidane, A., & Firoozabadi, A. (2014). An efficient numerical model for multicomponent compressible flow in fractured porous media. *Advances in Water Resources*, *74*, 127–147. https://doi.org/10.1016/j.advwatres.2014.08.010

Zidane, A., & Firoozabadi, A. (2021). Fickian diffusion in CO_2 injection: A two-phase compositional flow model with fully 3D unstructured gridding. *Fuel*, *303*, 121278. https://doi.org/10.1016/j.fuel.2021.121278

Zienkiewicz, O. C. (1982). Basic formulation of static and dynamic behaviours of soil and other porous media. *Applied Mathematics and Mechanics*, *3*(4), 457–468. https://doi.org/10.1007/BF01908222